

This item was submitted to [Loughborough's Research Repository](#) by the author.
Items in Figshare are protected by copyright, with all rights reserved, unless otherwise indicated.

A bistable rotary-translational energy harvester from ultra-low-frequency motions for self-powered wireless sensing

PLEASE CITE THE PUBLISHED VERSION

<https://doi.org/10.1088/1361-6463/aca4de>

PUBLISHER

IOP Publishing Ltd.

VERSION

VoR (Version of Record)

PUBLISHER STATEMENT

Original Content from this work may be used under the terms of the Creative Commons Attribution 4.0 licence. Any further distribution of this work must maintain attribution to the author(s) and the title of the work, journal citation and DOI.

LICENCE

CC BY 4.0

REPOSITORY RECORD

Masabi, Sayed, Hailing Fu, and Stephanos Theodossiades. 2022. "A Bistable Rotary-translational Energy Harvester from Ultra-low-frequency Motions for Self-powered Wireless Sensing". Loughborough University. <https://hdl.handle.net/2134/22284352.v1>.

A bistable rotary-translational energy harvester from ultra-low-frequency motions for self-powered wireless sensing

Sayed N Masabi, Hailing Fu*  and Stephanos Theodossiades

Wolfson School of Mechanical, Electrical and Manufacturing Engineering, Loughborough University, Leicestershire LE11 3TU, United Kingdom

E-mail: h.fu@lboro.ac.uk

Received 12 September 2022, revised 10 November 2022

Accepted for publication 22 November 2022

Published 8 December 2022



Abstract

This paper presents the design, theoretical modelling and experimental study of a bi-stable energy harvester (EH) using rotary-translation motion for ultra-low frequency and low excitation amplitude energy sources. A spherical magnet is adopted to produce the rotary-translational motion to convert ultralow-frequency kinetic energy into electricity over a wide frequency range. The bi-stable mechanism is realized by introducing two tethering magnets underneath the sphere magnet's oscillating path, significantly enhancing the operating range of the harvester. A theoretical model including the impact dynamics, magnetic interaction and electromagnetic conversion has been established to explore the electromechanical behaviours of the harvester under different operating conditions. The results illustrate that the EH operates in intra-well or inter-well motion depending on whether the input excitation is adequate to conquer the potential barrier depth. A prototype is developed to illustrate the design and to validate the theoretical model. The prototype generates sufficient power (mW) at frequencies lower than 2 Hz with excitation amplitudes as low as 0.1 g. A peak output power of 9 mW (1.53 mW RMS) is obtained at 2 Hz and 0.7 g with 750 Ω external load. The developed EH is integrated with an off-the-shelf power management solution to power a wireless sensing system to successfully record real-time temperature variation in the environment.

Keywords: energy harvesting, self-powered sensing, bi-stability, rotary-translational motion, nonlinear dynamics

(Some figures may appear in colour only in the online journal)

1. Introduction

Evolution of technology with the rise of Internet of things (IoT) has influenced the development and popularity of

wireless sensor network (WSN). The devices connected via IoT vary in terms of size and portability characteristics and such diversity requires WSNs to connect these devices to the internet [1, 2]. WSNs consist of a number of stationary or portable sensor nodes that communicate wirelessly to convey detected, processed and stored signals to their receivers, requiring uninterrupted power supply [3]. For this purpose, alkaline batteries have dominantly been used but they come with several drawbacks including their size, maintenance costs, hazardous components and limited lifecycle [4]. Duan *et al* [5] highlights the current limitations in WSNs

* Author to whom any correspondence should be addressed.



Original Content from this work may be used under the terms of the [Creative Commons Attribution 4.0 licence](https://creativecommons.org/licenses/by/4.0/). Any further distribution of this work must maintain attribution to the author(s) and the title of the work, journal citation and DOI.

and emphasizes that limited power available for sensors cause weak network communication life cycle and difficulties are faced with battery replacement for remote widespread sensors. In addition to the finite energy capacity of the batteries, their state of charge (SoC) cannot be easily predicted [6], which means they are often replaced before full depletion. Hence, to overcome these challenges, energy harvesting as an alternative to batteries has been considered as a promising solution [7, 8].

Energy harvesters (EH) are devices that convert ambient energy sources into electrical energy using various energy transduction mechanisms [9–11]. Siang *et al* [12] provides a taxonomy of potential energy harvesting sources where vibration sources fall under both ambient environment and external sources category. Amongst the other sources established such as solar, thermal, fluid and radio waves, vibration sources offer a clean, low maintenance method that is not reliant on climate conditions and can help preserve the environment in its original state [13]. Hence, vibration-based energy harvesting methods have gained popularity due to the availability and ease of energy conversion. In recent years, significant research attention was given towards utilizing vibration energy harvesting to power remote sensor nodes and address the major limited-energy-supply bottleneck of WSNs. The vibration energy used as input for energy harvesting can be obtained from machines, structures, vehicles, human motion and fluid flow [14]. The vibration energy can be characterized based on the dominant frequency content and noise of these sources and on whether the frequencies are stationary or non-stationary [15]. The human motion is considered as an external source of vibration and excitation from this type of motion are ideally dominant non-stationary frequencies. The main challenges faced while harnessing energy are regarding utilizing very low frequencies and effectively converting a wide range of frequency content available from these sources.

To address these problems, energy harvesters with various unique nonlinear vibration dynamics and transduction mechanisms have been established [16]. Kinetic generator dynamics can be classified based on different design approaches [17, 18] including multiple-degrees of freedom [19], frequency up-conversion [20, 21] and involving nonlinear mechanisms such as nonlinear restoring forces and multi-stability of the oscillating bodies. To maximize the power conversion, a combination of these nonlinear mechanisms and other principles such as stochastic resonance, end stoppers and Duffing nonlinearity can be used along with linear EH systems [22]. Wang *et al* developed a mono-stable EH using a rolling magnet with one fixed magnet to harness railway track vibrations ranging from 10 Hz to 400 Hz [23]. The capability of self-powered sensing for rail corrugation monitoring was successfully demonstrated. To utilize a wider range of frequencies and random excitation, multiple potential wells are implemented (using magnets [24] or manipulating the oscillating structure [25]) to create multi-stable oscillators [26]. Tran *et al* gives a comparison of different nonlinear techniques used for energy harvesting in [27]. Their work shows the significance of the bi-stable approach for improved performance under random

excitation and higher amplitude responses, while mono-stable designs perform comparatively poorly. Yildirim *et al* [28] also mentions the benefits of using bi-stability as a performance enhancement technique since it increases the power output, broadens the operating bandwidth without being influenced under white noise.

Vibration EH are also classified based on their energy transduction mechanisms, including piezoelectric [29], electromagnetic [30], triboelectric [31] and electrostatic transduction [32]. Among them, piezoelectric and electromagnetic harvesters have gained a great deal of research attention due to their high electromechanical coupling ability [33]. Piezoelectric EH (PEH) use deformations in cantilever beam-based structures to convert mechanical input into electrical energy [34]. Some low frequency PEH include systems with single [35] or multiple cantilever beam structures [36, 37], buckled-beam topologies [38, 39] and direct [40] and indirect plucking-based [21] (for example, excited by a revolving host) rotational architectures.

Electromagnetic generators have attracted significant attention in the research community for sensing applications, since they offer relatively higher power density, do not require additional power sources (electrostatic) to operate and are easy to integrate with sensing circuits [41]. Poulin *et al* [42] provides a comparison between piezoelectric and electromagnetic transduction mechanisms. Their study shows that although piezoelectric harvesters offer a higher power density, electromagnetic devices have much higher power output for devices with higher volume. Additionally, damping and natural frequencies of such devices can be adjusted by changing structural parameters, while for piezoelectric generators, the dielectric material itself has a large influence on these parameters which are more difficult to manipulate [43]. Zhang *et al* [44] proposed a rotational electromagnetic EH (EMEH) design capable of extracting a maximum output power of 3.2 mW with a low excitation input of 5 Hz and 30 Ω external load. A twist driving system and a ratchet clutch system were adopted. Yan *et al* [45] used the rotational mechanism along with bi-stability in their EMEH design. At 0.6 g excitation, the device performed in the interwell mode of oscillation at frequencies higher than 11.2 Hz, with maximum power output of 28 mW at 15.8 Hz with 2 k Ω external load. Oscillating bodies using translation have also been a popular approach for designing EMEH for low frequency applications. Fan *et al* [46] designed a 2-DoF device that uses magnetic levitation for human motion energy harvesting. Magnetic levitation has also been implemented in earlier research [47, 48], where spherical inertial masses have been used along with magnet-spring assembly to convert translational motion into electrical energy. Tao *et al* [49] have focused their study on enhancing the power density and efficiency of electromagnetic energy harvesting, and their micro scale device was capable of providing a maximum instantaneous power output of 244 μ W with 1 g excitations with 609 μ W cm⁻³. Hybrid EHs are also popular for broadening power conversion efficiency [31]. However, they come with complications regarding configuration

optimization, appropriate power optimization circuit to match load impedance with input impedance, complex design architectures and power output is still often marginally improved. Low frequency energy harvesting has been discussed across several literature using electromagnetic transduction but harnessing enough electrical output from ultra-low frequency mechanical excitation (e.g. <2 Hz) is still challenging for applications such as random human motion or turbine tower oscillations. Fu *et al* [50] proposed a concept of a bi-stable rotary-translational EH that uses motion of a rolling magnet as an inertial mass to convert mechanical energy into electrical energy, but this concept was not experimentally examined.

Hence, to deliver a practical solution for ultra-low frequency energy harvesting, this paper develops a novel bistable rotary-translational EH and establishes an enhanced theoretical model of the rotary-translational EH by considering impact dynamics of the rolling magnet, in order to study the electromechanical properties of the harvester and its performance under varying input excitation. A sphere magnet and a pair of tethering magnets are adopted to establish bistability to enhance the device's performance. The bistable dynamics in a rotary-translational EH is fabricated and studied for the first time to harness ultra-low frequency vibrations below 2 Hz and 1 g. To realize energy autonomy in the IoT, a self-powered sensing system for human temperature monitoring has been developed using the experimental prototype. The rest of this paper is organised as follows: section 2 introduces the working principle of the EH and theoretical modelling; section 3 illustrates the dynamics of the device under different operating conditions, analysing the effects of varying input excitation; the experimental setup, structural parameters and output performance of the EH are depicted section 4; section 5 presents a self-powered temperature sensing system that employs this EH as the power source; the conclusions are given in section 6.

2. Energy harvester design and theoretical modelling

This section explains the techniques used by the proposed rotary translational EH (RTEH) to harness low-frequency excitation and convert kinetic energy into electrical energy. The operating principle and assembly of the RTEH along with dynamic modelling will be discussed.

2.1. Design and operating principle

The schematic of the RTEH is presented in figure 1. A potential application of self-powered monitoring of wind turbines is illustrated in figure 1(a), where the ultra-low frequency harvester is mounted on a turbine tower to harness the oscillation energy of the turbine tower. A sphere magnet is contained within a cuboid casing, where the magnet can roll along the length of the casing, as shown in figure 1(b). The casing also provides end stops at either end of the sphere's rolling path. Underneath the rolling path, two tethering magnets are placed

such that the attracting forces between the rolling magnet and the tethered magnets can generate two stable positions for the system.

The magnetization direction of the tethering magnets is relatively reversed to create attractive forces at both stable positions. The distance between the tethering magnets is set as πr_m or 0.5 times the circumference of the sphere magnet, as labelled in figure 1(d). Consequently, as the sphere magnet moves from its resting position above one of the tether magnets and completes a half rotation, it switches the magnetization direction, and a second stable position is secured by the tethering magnet with reversed magnetization direction. This is demonstrated in figure 1(e), where a strong enough input excitation results in the sphere to conquer the potential well depth of its resting position and travel towards the right tethering magnet, rotating by 180° during its travel distance. Thus, two stable positions are secured on its rolling path and bistability is realized for the RTEH to harness ultra-low excitation inputs. To convert this motion into electrical energy, two copper coils are mounted directly on top of the sphere's rolling path, aligned with the tethering magnets. During oscillations, the sphere magnet rotates, causing change of the magnetic flux within the coils, which induces voltage through the electromagnetic induction.

The advantages of the proposed energy harvesting solution include: (a) the potential well of the harvester generated by the tethering magnets can be adjusted easily by changing vertical gap between the tethering magnets and the rolling magnet, allowing ultra-low frequency and low-excitation energy harvesting; (b) the rolling magnet-based design allows the system to operate at much lower frequencies compared to beam-based design; and (c) The unique magnetic restoring force provided by the tethering magnets allows the device to exhibit a special potential energy distribution, enabling the harvester to oscillate in a very large displacement range even under low-excitation conditions.

2.2. Governing equations

The equation of motion for the sphere magnet can be derived by considering its rotational and translational motion. Using Newton's second law of motion, as shown in figure 1(c), the following equation has been derived.

$$c_m \dot{\theta} r_m + \sum_{i=1}^n F_{\text{mag}}^i r_m - f_s - \hat{\Theta} I = m \ddot{x}, \quad (1)$$

where m and r_m are the mass and radius of the sphere magnet, $\dot{\theta}$ is the angular velocity, c_m is the damping coefficient, F_{mag}^i is the lateral component of the force due to the i th tethering magnet ($i = 1, 2$), $\hat{\Theta}$ is the electromagnetic coupling factor, I is the coil current, f_s is the static friction and \ddot{x} is the acceleration, which is also expressed as $r_m \ddot{\theta}$ (since $x = r_m \theta$). Assuming that the sphere rolls on its path without slipping, the torque is expressed as follows:

$$J \ddot{\theta} = f_s r_m, \quad (2)$$

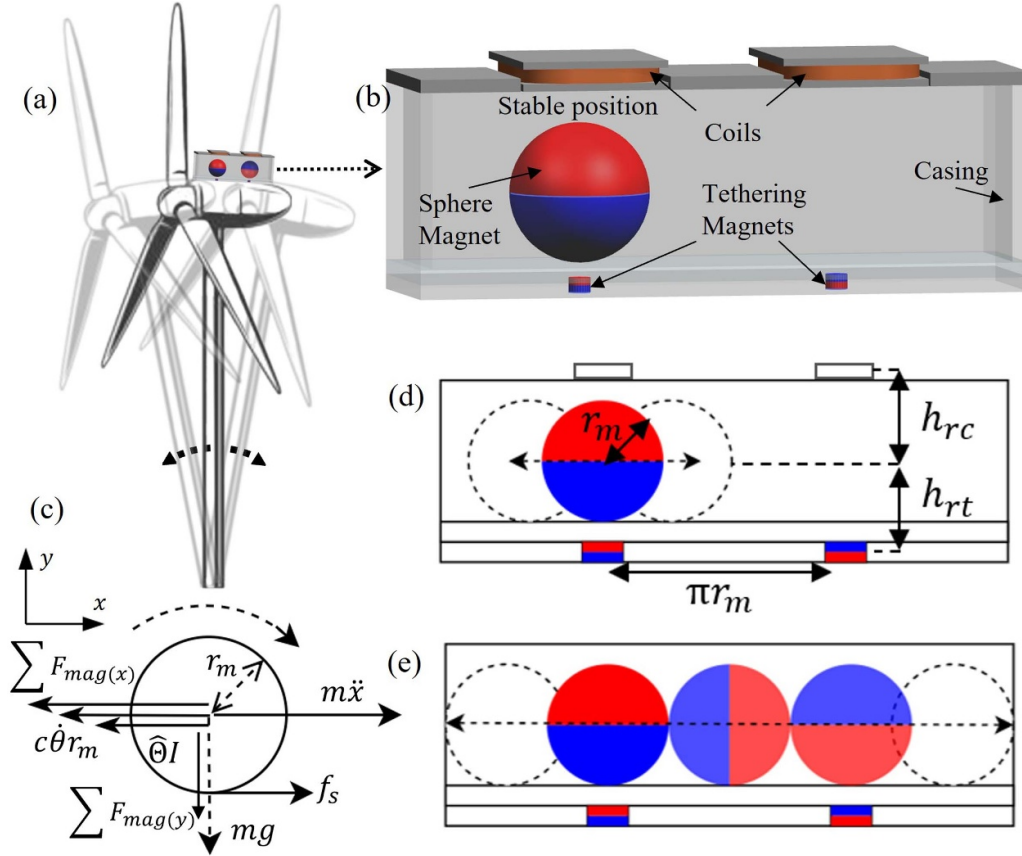


Figure 1. Self-powered applications in wind turbines (a) and schematic of the rotary-translational energy harvester (b), with freebody diagram of the sphere magnet (c), intra-well (d) and inter-well (e) modes of operation.

where $\ddot{\theta}$ is the angular acceleration and $J = \frac{2}{5}mr_m^2$ is the rotational inertia of the sphere magnet. Based on this expression of J and equation (2), equation (1) is expressed as follows.

$$\frac{7}{5}m\ddot{x} = c_m\dot{x} + \sum_{i=1}^n F_{\text{mag}}^i - \hat{\Theta}I \quad (3)$$

By considering the EH as a voltage source connected in series with internal impedance, the following equation can be derived using Kirchoff's voltage law:

$$L\dot{I} + (R_c + R_l)I - \hat{\Theta}v_m = 0, \quad (4)$$

where L is the coil inductance, $v_m = \dot{\theta}r_m$ is the translational velocity of the sphere, R_l and R_c are the load resistance and coil resistance, respectively. The lateral magnetic force F_{mag}^i from equation (3) can be modelled by considering the force exerted between the centre of masses of the rolling magnet and the tethering magnets due to their dipole moments [51]. This dipole-dipole interaction force can be modelled as follows:

$$F_{\text{mag}}^i = \frac{3\mu_0}{4\pi r^5} \left[(m_r \cdot r_i)m_t + (m_t \cdot r_i)m_r + (m_r \cdot r_i)r_i - \frac{5(m_t \cdot r_i)(m_r \cdot r_i)}{r_i^2}r_i \right] \quad (5)$$

where r_i is the distance between the sphere and i_{th} tethering magnet ($i = 1, 2$), μ_0 is the permeability of free space or magnetic constant, m_r and m_t are the dipole moments of the rolling and tethering magnets, respectively. Expressions for the magnets can be given as follows:

$$m_r = \frac{4Br}{3\mu_0} \pi r_m^2 [r_m \sin(\theta), 0, r_m \cos(\theta)] \quad (6)$$

$$m_t = \frac{Br}{\mu_0} \pi r_t^2 [0, 0, t_{th}/2], \quad (7)$$

where Br is the residual magnetic flux density and its equation is established in [50]. The distance between the left and right tethering magnets and the sphere magnet is given by:

$$r_1 = \left[\theta r_m - \frac{1}{2} \pi r_m, 0, h_{rt} \right] \quad (8)$$

$$r_2 = \left[\theta r_m + \frac{1}{2} \pi r_m, 0, h_{rt} \right], \quad (9)$$

The electromotive force (emf, $\epsilon = \hat{\Theta}v_m$) induced in the coils is equal to the rate of change of the magnetic flux passing through the coil

$$\epsilon = \frac{d\Phi_m}{dt} = \frac{d\Phi_m}{ds} \frac{ds}{dt} = \frac{d\Phi_m}{ds} v_m = \hat{\Theta}v_m. \quad (10)$$

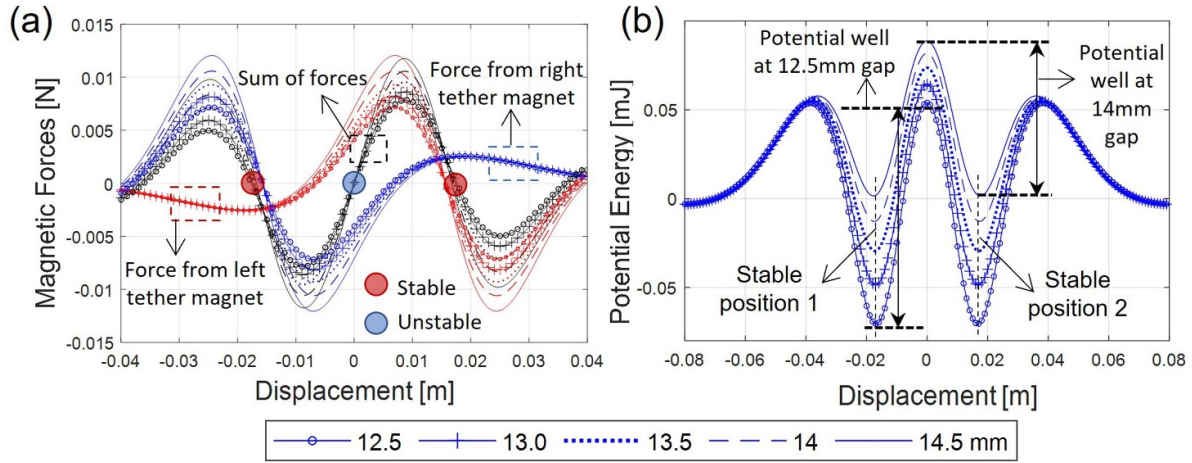


Figure 2. Tethering magnet force (a) and potential energy (b) profiles.

The electromagnetic coupling coefficient $\hat{\Theta}$ represents the rate of change of magnetic flux through the coils with respect to the translational displacement of the rolling magnet. The magnetic flux passing through the coils can be calculated by [52].

Since the inertial mass will face two impact zones while oscillating in the inter-well motion, it is important to define conditions for the velocity profile of the sphere before and after impacts. It has been established that the sphere can rest in equilibrium in two stable positions where the tethering magnets are situated. By setting the centre of the rolling path as the reference where the sphere starts oscillating upon excitation, the conditional statements for the sphere's displacement can be represented as follows.

$$v_m = \begin{cases} v_{m0}, & \text{when } |\theta| < 0.5L_{rm} \\ -ev_{m0}, & \text{when } |\theta| \geq 0.5L_{rm} \end{cases} \quad (11)$$

where v_m is the velocity of the sphere after considering the influence of the impacts, v_{m0} is the velocity of the sphere before impacts, L_{rm} is the length of the rolling path and e is the coefficient of restitution.

3. Dynamics of the energy harvester

A numerical model is developed in MATLAB based on the governing equations established in section 2.2. Different input excitation conditions, sizes of components and gaps between the rolling and tethering magnets are considered for investigating the dynamics and electrical performance of the EH. The potential energy and force profiles of the rolling magnet are established by considering the force components on the horizontal axis applied by the tethering magnets, as depicted in figure 2. From the combined force profile represented by the black lines (figure 2(a)), two sinusoidal waves represent the attractive forces offered by the tethering magnets. The areas where the magnetic forces equal zero are the stable equilibrium positions (as depicted by the red dots in (figure 2(a))). The stable positions are further illustrated in figure 2(b) through

the potential energy of the rolling magnet against displacement. The depth of the potential barriers can be varied easily by changing the vertical distance between the tethering magnets and the sphere magnet; this is illustrated as the amplitudes of the potential energy and magnetic forces vary as the vertical magnetic gap is changed between 12.5 mm to 14.5 mm.

With the established potential wells on the rolling path, the sphere magnet can oscillate in a few distinguishable operating modes. If the input excitation is low, the sphere's kinetic energy is not enough to conquer the potential barrier created, and hence it oscillates near a tethering magnet. This type of motion is called the intra-well motion as shown in figure 1(d). For high excitation, the energy of the sphere is higher than the depth created by the tethering magnets, and it can oscillate across the full length of the rolling path, thus achieving the inter-well motion. Chaotic motion is expected when the sphere's maximum kinetic energy matches with the potential barrier depth, which causes the inertial mass to travel chaotically between two stable positions.

The magnetic flux density distribution of the rolling magnet at the mid-point of mounted coils is given in figure 3. Figures 3(a) and (b) shows the magnetic flux density distribution in the left coil, and that of the right coil is depicted in figures 3(c) and (d). In figure 3(a), the vertical magnetic flux density is positive and maximum at $-0.5\pi r_m$. As the polarity reverses at $0.5\pi r_m$, the negative peak with same amplitude occurs, as seen in figure 3(c). In figures 3(b) and (d), it can be seen that the amplitude of flux density at the coil centres reduces as a result of increasing the vertical gap between the coils and the rolling magnet. Finally, the combined magnetic flux density profile of both coils is shown in figures 3(e) and (f). When the rolling magnet oscillates between two sets of coils, the maximum magnetic flux density occurs when the rolling magnet is passing by the coils, generating the maximum change of magnetic flux and improved output power.

Figure 4 presents the dynamic behaviour of the EH under three different excitation amplitudes at 2 Hz excitation frequency, generated using the numerical model. For the same frequency, intra-well (figure 4(a)), chaotic (figure 4(d)) and

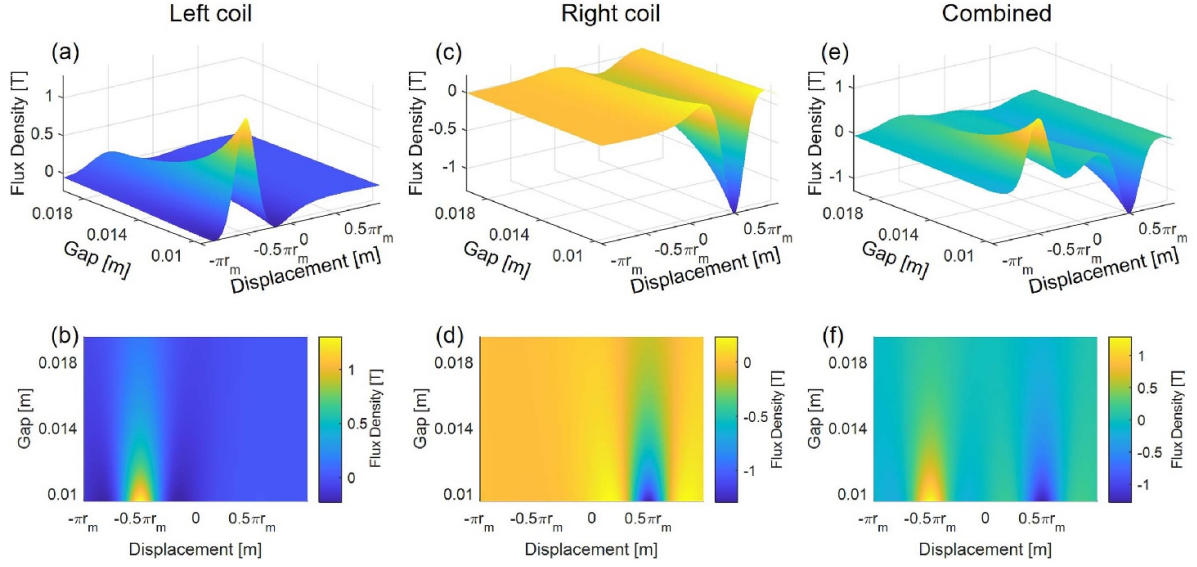


Figure 3. Magnetic flux density distribution of the rolling magnet: vertical component of magnetic flux density on the left coil (a) and (b), right coil (c) and (d) and their combined profile (e) and (f). Increasing the gap between the coils and the rolling magnet reduces the flux density, as seen in (b), (d) and (f).

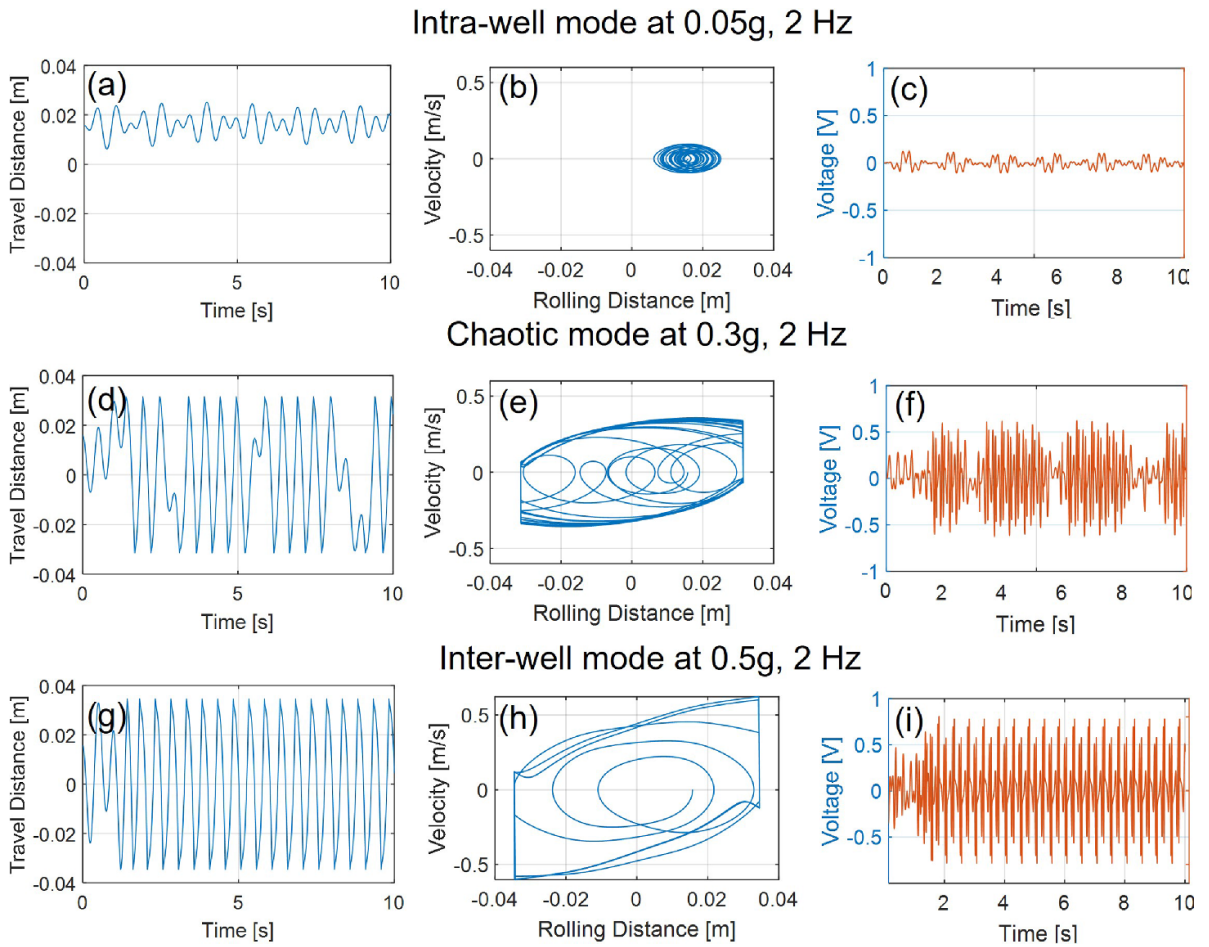


Figure 4. Theoretical investigation of sphere magnet's displacement time history, phase portraits and voltage output across the coils with external load at 2 Hz excitation. Intra-well motion (a)–(c) at 0.05 (g), chaotic inter-well motion (d)–(f) at 0.3 (g) and periodic inter-well motion (g)–(i) at 0.5 (g) are presented.

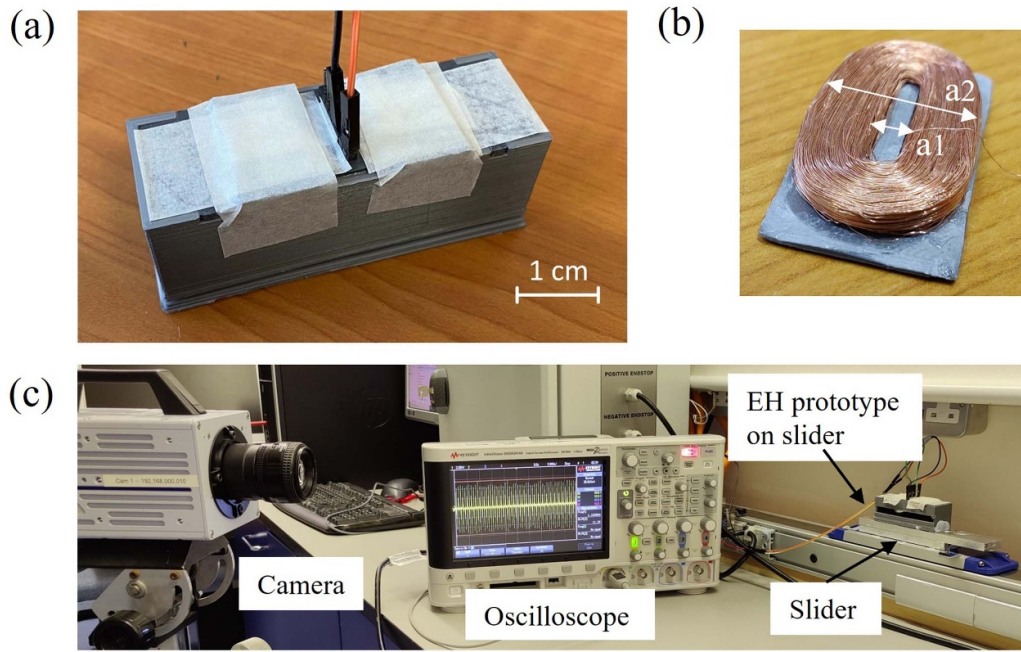


Figure 5. Physical prototype (a), copper coil (b) and laboratory setup (c) including prototype on a vibration simulator, oscilloscope and a high frame rate camera.

periodic inter-well (figure 4(g)) motions are obtained with different excitation amplitudes. The output voltage depicted in figure 4(c) is relatively low since the sphere magnet oscillates below one of the two mounted coils in the intra-well mode with small travelling displacement and velocity amplitudes. During the inter-well motion, it is apparent from figures 4(f) and (i) that the output voltage amplitude is enhanced and the voltage frequency is higher than the input excitation frequency or the displacement frequency in figures 4(d) and (g). This frequency amplification occurs due to the effectively designed coil-magnet orientation. The magnetic flux density varies three times during each half cycle of sphere's rotation during the inter-well motion, which results in the output voltage frequency of the device to occur six times the input excitation frequency. This ratio can be varied by changing the electromagnetic coupling factor, which relies on the gap between the coils and the sphere magnet.

4. Prototyping and experimental study

4.1. Experimental setup

An energy harvesting prototype is fabricated and assembled, as shown in figure 5(a) to validate the design and the theoretical model. The casing for the harvester was 3D printed with indents on the rolling track for the neodymium iron boron (NdFeB) tethering magnets to be fitted. The gap between the rolling and tethering magnets was kept constant but it can be adjusted by placing printed thin plates of different thickness between them to vary the strength of the tethering forces. A spherical NdFeB magnet of dimensions as shown in table 1 was placed in the casing and two copper coils of identical properties (see figure 5(b)) were mounted above the rolling

Table 1. Design parameters and material properties.

Symbol	Description	Value
m	Sphere magnet mass	29.4 g
ζ	Mechanical damping ratio	0.046
r_m	Sphere magnet radius	10 mm
B_r	Residual flux density	1.3 T
r_t	Tethering magnets' radii	1.5 mm
l_t	Tethering magnet height	2 mm
h_{rt}	Vertical gap between sphere and tethering magnet	22 mm
h_{rc}	Vertical gap between sphere magnet and coil	12 mm
a_1	Coil inner width	3 mm
a_2	Coil outer width	12 mm
a_3	Coil outer length	20 mm
L_{rm}	Sphere magnet's travelling length	60 mm
L	Coil inductance	152.7 mH
R_c	Coil resistance	380 Ω
e	Coefficient of restitution	0.4

path and connected in series. The coils were fabricated using a manual winding machine where they were fed around a clamped metal slit, resulting in the oval shape instead of circular geometry as represented in the theoretical modelling. An equivalent circular shape was adopted in the numerical study to ensure the close match between the experimental and numerical results.

The fabricated prototype was fixed on a slider platform powered by a Kollmorgen EN60034 servomotor to simulate low-frequency input excitation up to 2 Hz, given that the displacement was within the range of the slider's length. The

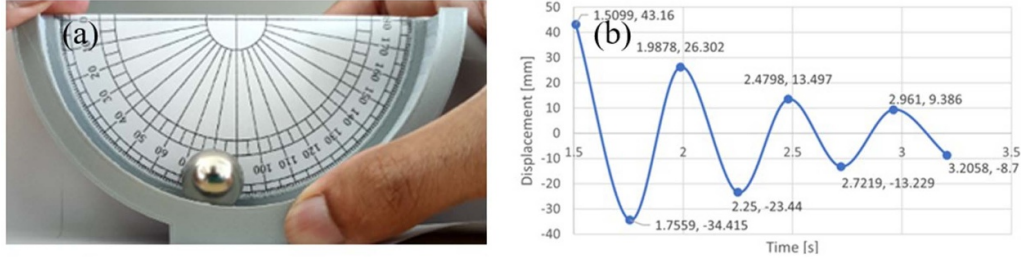


Figure 6. Damping measurement test setup (a) and displacement against time graph (b) to calculate damping parameters.

slider was controlled by a Kollmorgen variable frequency drive. To understand the electrical properties, the voltage output from the coils were recorded using an oscilloscope. In order to analyse the mechanical properties of the rotary-translational sphere magnet, an incision was made on the casing to partially expose the sphere. The sphere's full range of motion relative to the casing was visible through the window and it was recorded using a Photron FASTCAM SA3 high-speed camera (labelled in figure 5(c)). An accelerometer was also used to capture the casing's motion.

4.2. Determination of motion parameters

The damping ratio was measured using the experimental setup shown in figure 6. The sphere magnet was allowed to freely oscillate on a wide arched path fabricated using the same material as that of the harvester casing. The displacement data shown in figure 6(b) was used to calculate the damping coefficient c as follows:

$$c = \frac{\delta}{\sqrt{4\pi^2 + \delta^2}} = 0.0351 \text{ kg s}^{-1}, \quad (12)$$

where δ is the logarithmic decrement expressed as:

$$\delta = \frac{1}{n} \log \left(\frac{x(t_0)}{x(t_n)} \right) = 0.221, \quad (13)$$

where n is the number of peaks, $x(t_0)$ and $x(t_n)$ are the first and final peak displacements. Finally, the damping ratio can be derived as follows:

$$\zeta = \frac{c}{2m\omega_n} = \frac{c}{2m \cdot \frac{\sqrt{4\pi^2 + \delta^2}}{(t_n - t_0)/n}} = 0.046, \quad (14)$$

where ω_n is the resonant frequency, t_0 and t_n are the first and final peak displacement periods. With the coefficient of restitution and damping ratio measured and the other physical parameters of the prototype confirmed, the theoretical model was tuned to validate the experimental results.

In order to determine the energy lost during hard impacts between the sphere magnet and the casing end stops of the rolling path, the dynamic behaviour of the sphere magnet is investigated by observing impacts between the sphere magnet and the inside end walls of the fabricated casing. With the information obtained from figure 7, the characteristics of the sphere before and after collisions can be quantified. The coefficient of restitution (COR) is a parameter used to

characterise collisions between objects and is quantified by values between 0–1. It is defined as the ratio of the velocity after the separation of two bodies to the velocity before impact [53]. COR can be expressed as follows:

$$e = \frac{v_2}{v_1} \quad (15)$$

where v_2 and v_1 are the velocities after and before impact and e is the COR. As discussed earlier, two stable equilibria of this device means the system can perform in intra-well and inter-well modes of oscillations. During the periodic inter-well motion, since the sphere magnet can travel the full range of motion provided by the rolling path, impacts are apparent between both ends of the casing and the sphere. The incident and rebound velocities of the sphere was measured by recording its motion at a high frame rate. Using an average of COR measured at both hard impact zones before and after collision, the mean value for COR was calculated as 0.401.

4.3. Results and discussion

For different input excitation levels, the harvester oscillates in different modes, including intra-well, chaotic double-well and periodic double-well oscillation modes, as illustrated in figure 7. During each test, the device was excited from stationary state, and the rolling magnet is initially resting in one of the stable positions. When there is input excitation, the rolling magnet starts oscillating from said resting positions. At 2 Hz and 0.1 g, figure 7(a) shows repeatable intra-well motion since the sphere magnet oscillates near one of the tethering magnets and is unable to conquer its barrier depth, hence the displacement profile shows low amplitude motion (<30 mm). At slightly higher amplitudes in figures 7(b) and (c), intra-well motion with occasional inter-well movements is apparent as the rolling magnet occasionally travels between the stable positions and the inter-well motion becomes more frequent at 0.3 g. At 0.4 g in figure 7(d), hard impacts against both ends of the casing are visible and the oscillations between stable positions become more frequent at 0.5 g (figure 7(e)). At 0.6 g (figure 7(f)), the sphere continues to travel between two stable regions, taking advantage of the full range of motion to maximize the rate of change of the magnetic flux and to enhance the energy harvesting performance.

Figure 8 presents open-circuit voltage from the RTEH prototype under varying excitation conditions to show how output voltage behaves under different excitation frequencies. The

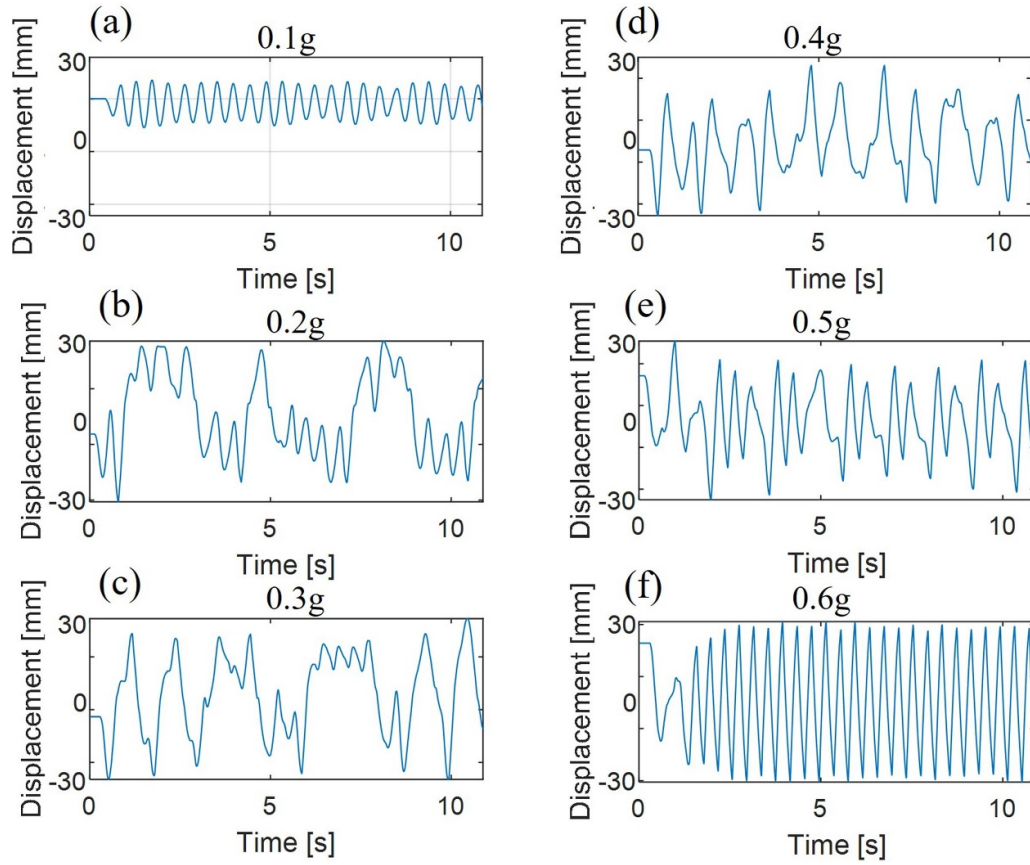


Figure 7. Tracked motion history of the sphere magnet at 2 Hz excitation frequency at 0.1 g–0.6 g (a)–(f) amplitude. The operation modes of the harvester transitioning from intra-well to chaotic inter-well to periodic inter-well motion is observed.

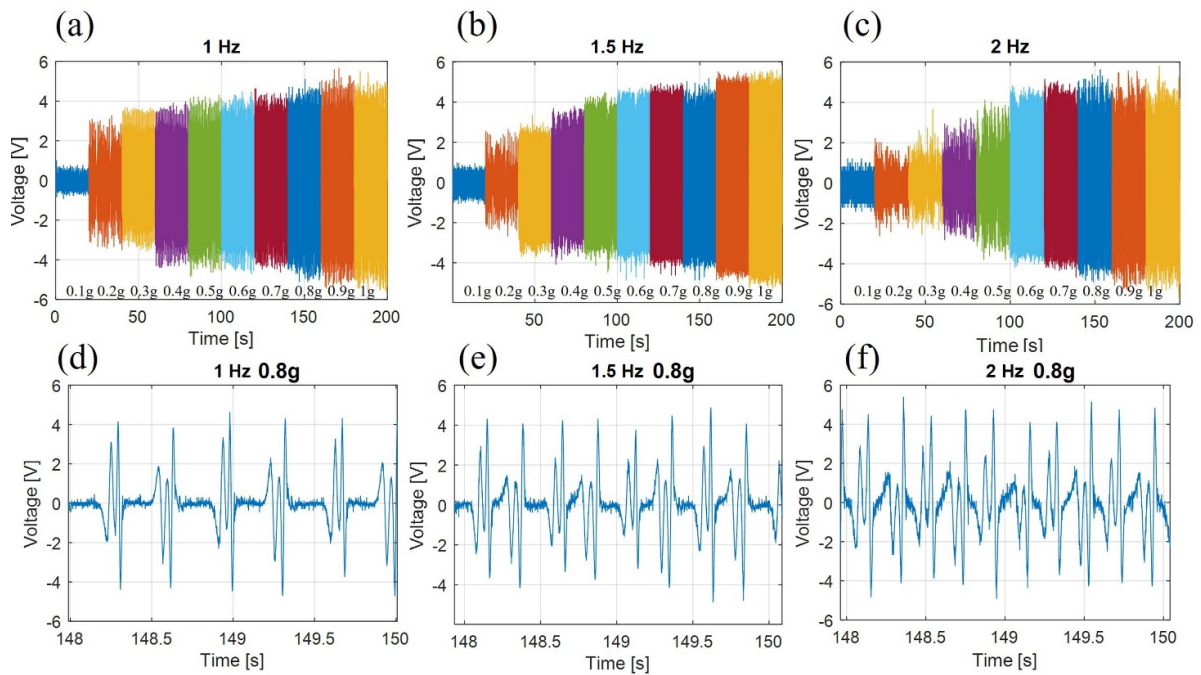


Figure 8. Open-circuit voltage under 0.1 g–1 g at 1 Hz (a), 1.5 Hz (b) and 2 Hz (c). (d)–(f) details of the output voltage at 0.8 g for different excitation frequencies.

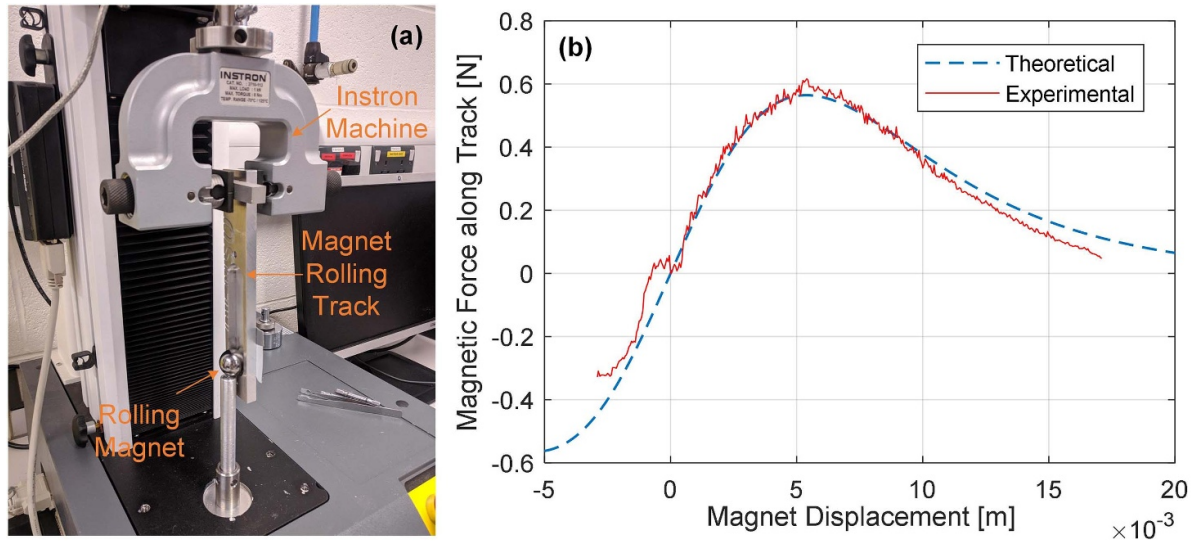


Figure 9. Validation of the magnetic force calculation using the dipole model. (a) Testing rig with an Instron machine; (b) comparison between the theoretical and experimental results against rolling magnet displacement.

output voltage profiles from figures 8(a)–(c) shows that the output voltage increases as the excitation amplitude increases, indicating that the rolling magnet transitions from intra-well to inter-well motion, especially for those regions where the output voltage has sharp changes. In figure 8(a), it is apparent that the inter-well motion occurs from 0.2 g onwards at 1 Hz while it requires over 0.5 g amplitudes to behave periodically at 2 Hz in figure 8(c). However, figures 8(d)–(f) demonstrates that higher input frequency results in output voltage also having a proportionally higher frequency, resulting in greater average voltage.

4.4. Comparison between the numerical and experimental results

The magnetic force between the rolling magnet and the tethering magnet is calculated using the dipole model as shown in equation (5). In order to examine the capability of this model, the magnetic force was tested using an Instron machine and a testing rig with the rolling and tethering magnets mounted in the same way as those in the RTEH prototype, as shown in figure 9(a). The Instron machine can accurately capture the applied forces to counterbalance the magnetic force along the rolling path for different displacement. The comparison between the theoretical and experimental results is shown in figure 9(b), and a good match is obtained, especially for the range near the peak value.

In order to validate the theoretical model for the RTEH design, a comparison between the numerical and experimental output voltage results with fixed resistive external load is illustrated in figure 10 for the harvester operating between excitation amplitudes of 0.1 g–0.9 g at 2 Hz excitation frequency. The trend of increasing peak-to-peak voltage for higher input amplitudes is very similar between figures 10(a) and (b). However, the prototype behaves optimally at 0.7 g excitation

amplitude and at higher amplitudes, the harvested output plateaus. In addition, the experimental results are a bit unstable and noisy compared to the numerical results which is quite repeatable.

Several reasons that lead to the differences between the experimental and numerical results are discussed below: (a) input excitation noise from the low-frequency slider in the experimental setup, as shown in figure 10(c), (b) uneven 3D printed rolling surface of the prototype, (c) impacts of the rolling magnet on the harvester casing. These factors are not included in the theoretical model. Although there is some mismatching between the experimental and numerical results, the theoretical model can still describe the system dynamics overall.

For the results in figure 10, the EH was connected with a 750 Ω resistive load, matching the internal impedance of the device for maximum power output. This optimal resistance was obtained in an impedance matching test, as shown in figure 11. The orange curve shows the trend of output power as a result of changing load resistance when the prototype is given fixed input excitation of 0.7 g amplitude and 2 Hz frequency, and as highlighted, maximum power of 6.8 mW is extracted at 750 Ω .

Figure 12 illustrate the comparison of the numerical and experimental results for different excitation amplitudes and frequencies. A good match was obtained between these results, validating the theoretical model. Intra-well motion at 0.1 g shows oscillations with relatively higher amplitudes in theory in figures 12(a) and (b), compared to experimental displacement trace in figures 12(c) and (d). Figures 12(e)–(h) show that for periodic inter-well motion, the characteristics are mostly congruent. At periodic inter-well mode of operation, the results offer a very reliable match and are comparable. In figures 12(i) and (j), two comparable full cycles followed by a half cycle voltage during a half cycle of the sphere's oscillation is apparent from both experimental and numerical

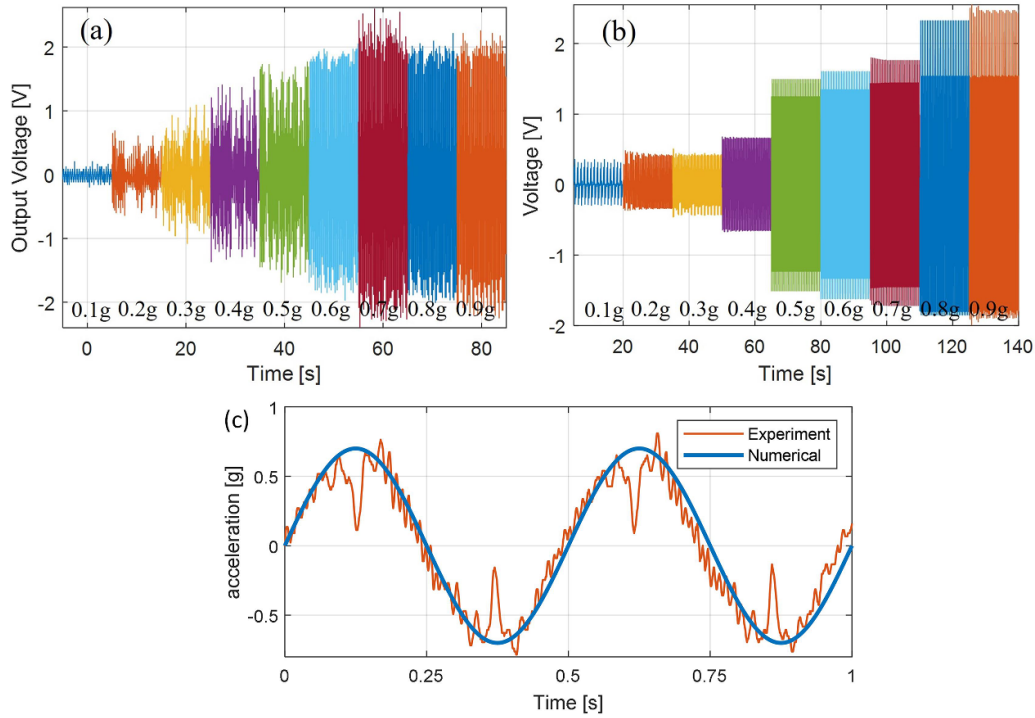


Figure 10. Experimental (a) and numerical (b) voltage output for various excitation amplitudes with $750\ \Omega$ external load; (c) comparison of input excitation used in experimental testing and numerical study (0.7 g and 2 Hz).

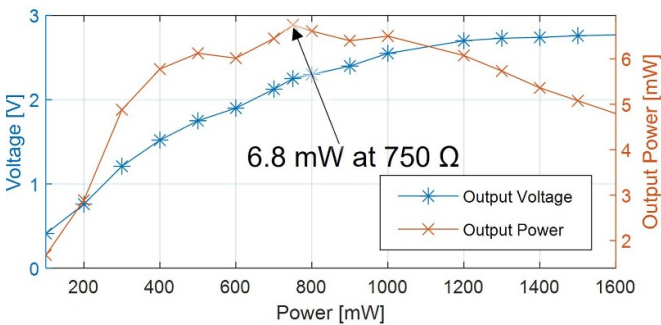


Figure 11. Output power and voltage as a result of varying external load resistance between $100\ \Omega$ – $1600\ \Omega$. Maximum power is obtained at $750\ \Omega$ where load matches the internal resistance of the energy harvester.

time histories, and the pattern of the output reverses as the sphere magnet travels backwards during the second half of the oscillation.

In figures 12(i) and (j), the experimental and numerical results are slightly different at 60.4 s and 60.6 s. As discussed earlier, the main reasons include (a) input excitation noise from the experimental setup, as shown in figure 10(c), (b) uneven rolling surface of the sphere, (c) impacts of the rolling magnet. However, the overall trend and amplitudes are very close, showing the validity of the theoretical model.

4.5. Parametric study

To illustrate the capability of the RTEH under broadband low excitation inputs, its crucial to undertake a parametric

investigation. In figure 13, bifurcation diagrams are presented for excitation frequencies of 1 Hz in figure 13(a), 1.5 Hz in figure 13(b) and 2 Hz in figure 13(c). For each of these input frequencies, the numerical model is tested under excitation amplitudes between 0–1 g acceleration to observe periodic and chaotic behaviours and to establish the optimal conditions to harness vibrations.

At 1 Hz (figure 13(a)), chaotic behaviour was observed initially between 0.01 g–0.04 g and following that the system resumes periodic inter-well oscillations. At high amplitudes with 1 Hz input, the system is mostly stable since the impacts between the end barriers and the sphere magnet are repeatable, resulting in stable oscillations without chaos. The system behaves mostly stable with a chaotic region between 0.1 g–0.23 g at 2 Hz. The chaos is apparent since at low excitation, the sphere often travels between potential wells with occasional collisions at the impact zones, as shown in figure 13(c). At 1.5 Hz, although the system is mostly stable from 0.1 g onwards, chaotic operation can be observed between 0.7 g–0.88 g region, before the system stabilises again. The system seems chaotic since the sphere magnet's travelling acceleration changes gradually while it conquers the potential barrier depth created by the tethering magnets.

The restoring forces created from the hard impacts from the casing is also responsible for this chaotic region. To explain the seemingly chaotic behaviour, the phase portraits from the chaotic regions are generated in figure 14. In figure 14(a), chaotic behaviours can be observed. The rolling magnet oscillates within the casing randomly. In figures 14(b)–(d), the phase portraits show that although these excitation amplitudes seemed chaotic in figure 13(b), the sphere does oscillate in

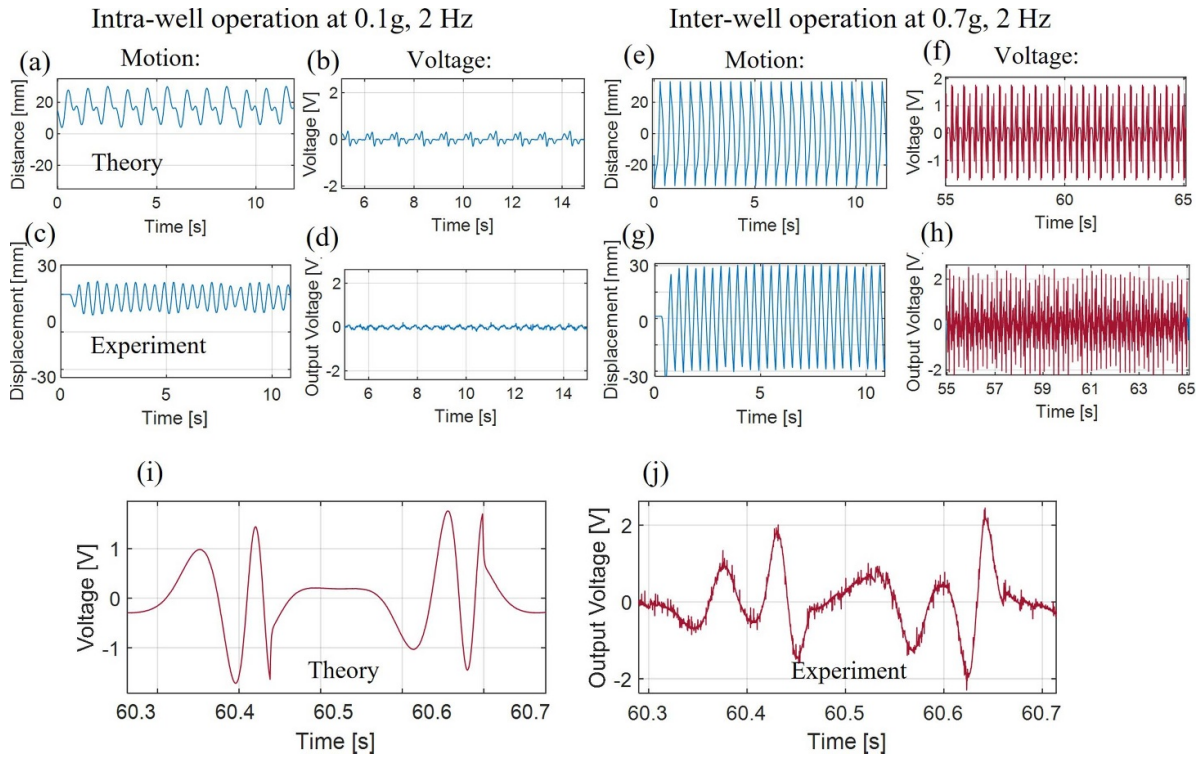


Figure 12. Comparison of sphere magnet displacement and voltage output between experimental and theoretical results. Intra-well (a)–(d) and inter-well (e)–(h) modes are compared. The output voltage cycles for one period of sphere's oscillation is also compared at 0.7 g (i)–(j). Input frequency is kept constant at 2 Hz.

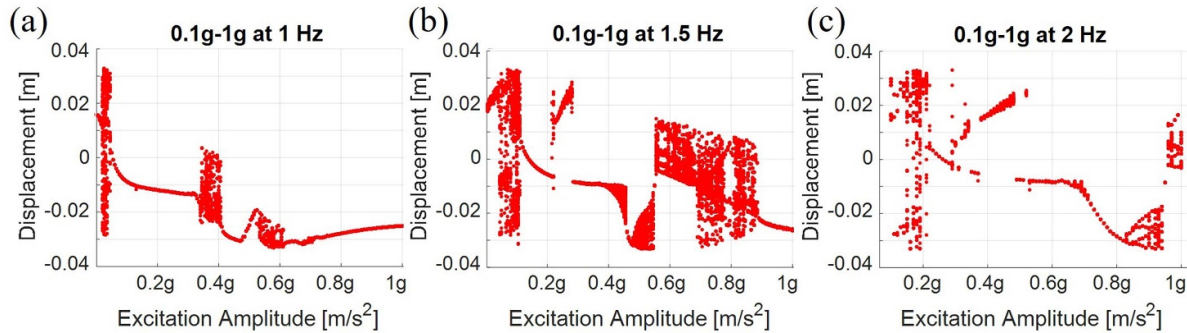


Figure 13. Bifurcation diagrams for varying excitation amplitudes at 1 Hz (a), 1.5 Hz (b) and 2 Hz (c).

periodic inter-well motion. This is further supported using the voltage histories in figures 14(e)–(h), corresponding to the excitation inputs used in figures 14(a)–(d) respectively. The bifurcation diagram shows chaos since the travelling velocities change due to the influence of the impact. Additionally, at higher amplitudes (figures 14(c) and (d)), a second small impact is often visible as the sphere reaches either ends of its rolling path, which also contributes to the chaotic behaviour.

In order to further examine the optimum operating conditions of the proposed EH, parametric studies are performed to evaluate the output power characteristics for varying excitation inputs and changing the gap between the tethering magnets and the rolling magnet in figure 15. In figure 15(a), the outcome of frequency sweep between 0.4 Hz to 2 Hz with fixed excitation amplitude of 0.8 g for with different vertical

magnetic gaps are illustrated. Changing the vertical gap allows the strength of the potential energy wells created by the tethering magnets to be varied; increasing the gap weakens the attractive forces and the restoring forces from the end stops are more dominant. The effect of the vertical gap on the output power can be understood further in the projected map in figure 15(b) with labelled parameter space A, B and C. Region A with the blue area within 1.5 Hz–2 Hz and 4 mm–9 mm vertical gap shows gradual increase in power as a result of increasing both frequency and vertical gap (in effect reducing potential energy well strength and attractive forces from the tethering magnets towards the sphere magnet). The behaviour indicates that the rolling magnet operation transitions from intra-well to inter-well mode with hard impacts. This phenomenon is also present in region C, as represented between 0.4 Hz–1.3 Hz for the full range of vertical gap

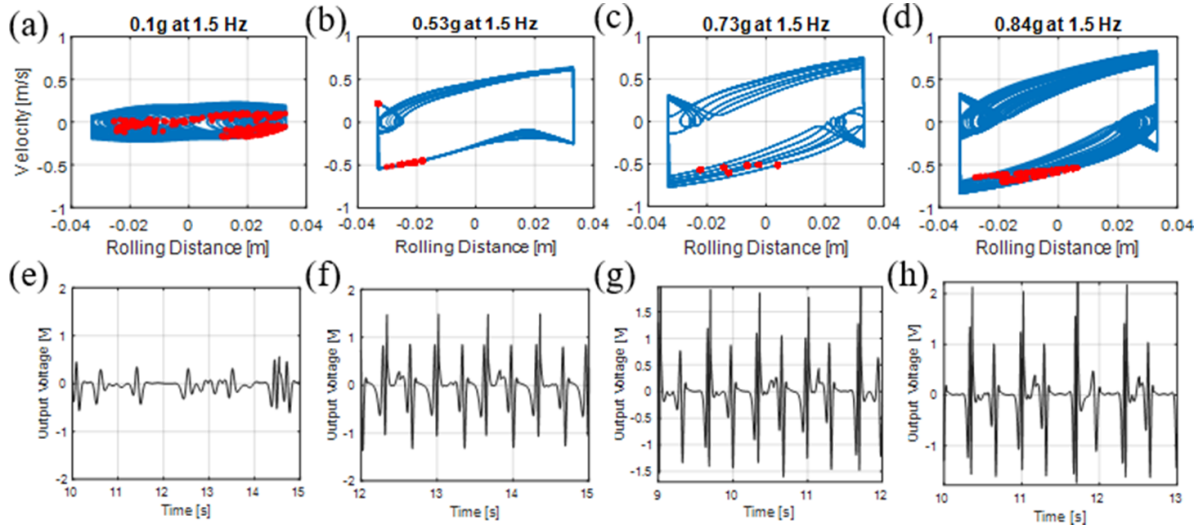


Figure 14. Phase portraits and associated voltage outputs from chaotic regions in 1.5 Hz bifurcation plot from figure 13 at 0.1 g (a) and (e), 0.53 g (b) and (f), 0.73 g (c) and (g) and 0.84 g (d) and (h).

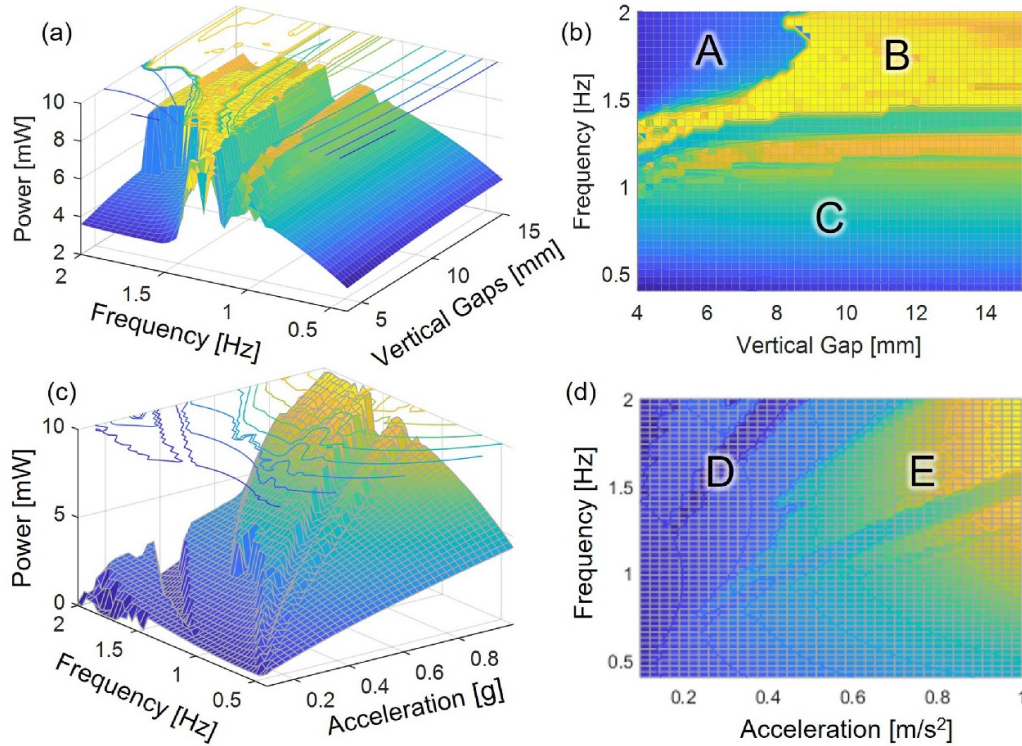


Figure 15. Power output of the energy harvester for a frequency sweep of 0.4 Hz–2 Hz at different vertical magnetic gaps (a), with a projected map (b) conforming of regions A, B and C to represent the following modes of operation: intra-well, inter-well with impact and inter-well without impact respectively. (c) Power output versus excitation frequency and amplitude and (d) its projection. D and E indicates different oscillation conditions.

considered. The orange region in space C indicates that the device is operating in inter-well mode with stronger impacts against the end stops provided by the casing. Most optimal operating conditions are present in the yellow space in the map labelled as region B, as the output power plateaus around a maximum value of 7.9 mW. The hard impacts occurring due to the presence of the casing causes the slight fluctuations in output power, and implies that the rolling magnet is travelling with inter-well operating mode with impacts (utilizing the full

length of available rolling path) throughout this region. With fixed vertical gap of 11 mm and same frequency sweep range used in figure 15(a), the output power behaviour is derived for an excitation range of 0.1 g–1 g amplitude in figure 15(c). As expected, a general trend of increasing power up to 10 mW is observed as excitation inputs are increased. In figure 15(d), two more parameter spaces D and E are labelled to represent the effects of restoring forces from impacts on the output power, which are dominant in region E compared to D.

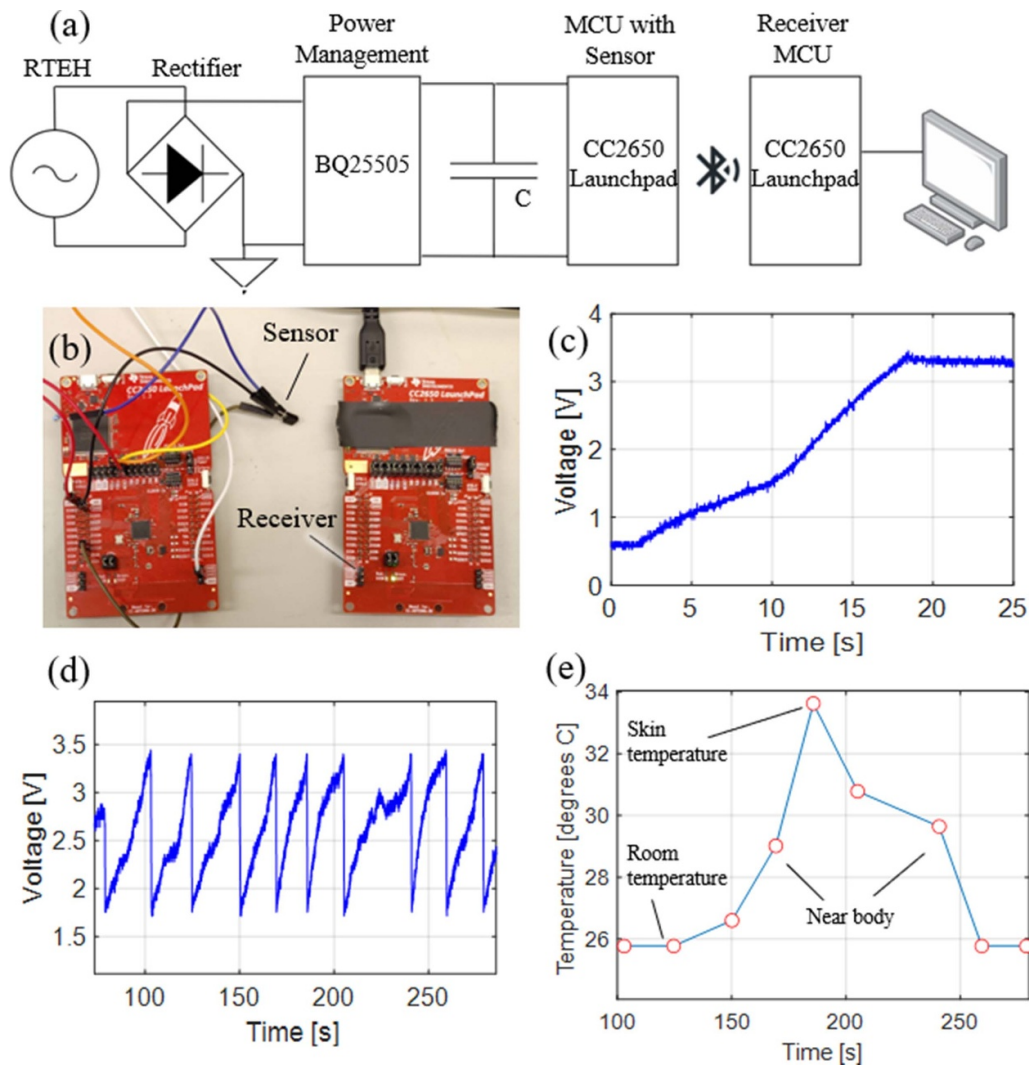


Figure 16. Energy harvester used to power a temperature sensor wirelessly to monitor human body temperature (a). Capacitor-powered receiver MCU turns on (receiver LED in (b) blinks to indicate this) when capacitor fully charged to 3.3 V (c). Reset trigger cycle (d) allows the capacitor to recharge between temperature readings (e).

5. Self-powered sensing application

To illustrate the applicability of the RTEH prototype, the generated output from the EH is used to power a wireless sensor to monitor the temperature from surroundings and to send the data to a wireless receiver using Bluetooth. Such a self-powered sensing setup is represented in the schematic shown in figure 16(a). In order to convert the alternating voltage supply from the EH to DC voltage, a Schottky diode full-bridge rectifier is employed. The DC voltage is then used as the input for a BQ25505EVM power management board consisting of a boost converter, used to step-up the voltage to a required 3.3 V. This enhanced output is then used to charge a $330\ \mu\text{F}$ capacitor C effectively, as shown in figure 16(c). When sufficient energy is stored in the capacitor, the BQ25505 board generates a trigger signal to a Texas Instruments CC2650 micro-controller unit (MCU) that enables control of the reset mode of the MCU, as shown in figure 16(b). Tprogrammed

such that when C charges up to 3.3 V, the MCU turns on and automatically turns off if C discharges to 1.8 V, allowing it to charge back up to 3.3 V. This cycle continues as long as C is being charged up. An LMT85LP temperature sensor is connected to the MCU such that it can power the sensor and read the output from the sensor through an ADC channel. A second CC2650 MCU is added to the setup to act as a receiver. The receiver MCU is connected to a computer and whenever it receives data from the first MCU, it is converted into temperature reading using a conversion program setup in MATLAB.

Figure 16(c) shows the boost converter output charging up capacitor C up to a steady 3.3 V. The charging and discharging pattern is illustrated in figure 16(d) and temperature readings corresponding to the 3.3 V peaks when the transmitter MCU turns on in real time is presented in figure 16(e). The obtained data in figure 16(e) shows the change in temperature as the sensor is on a desk, near human body, touching a

fingertip and cooling down back to room temperature when kept on desk. The recorded room temperature was 25.7 °C and skin temperature of the test subject was around 33 °C, which corresponds with the values collected by the LMT85LP temperature sensor powered by the developed RTEH. Figure 16(b) shows the receiver MCU receiving instantaneous data via Bluetooth when the capacitor voltage reaches 3.3 V. The capacitor was charged while the RTEH was exposed to 0.8 g and 2 Hz vibrations. The recharging periods in figure 16(d) shows that the capacitor takes between 15 to 45 s to recharge once. Then the capacitor is depleted to 1.8 V after power is consumed by each sensing cycle. The varying period was caused since the prototype occasionally travelled in the intra-well mode due to random energy loss, which resulted in dips in the output power, and in turn causing in a delay in recharging of the capacitor.

In terms of wireless communication distance, two CC2650 launchpad micro-controllers were used for the purpose of transmitting sensed temperature data using Bluetooth low energy 5.1, and several meters wireless data communication distance was realized in lab environment. From the literature [54], the wireless data communication range for Bluetooth 5.1 is 10–100 m.

6. Conclusions

A bi-stable rotary-translational EH is developed in this paper using an enhanced theoretical model. Rotary-translational motion of a sphere magnet is adopted to harness ultra-low frequency random vibrations. Bi-stability is realised by employing two tethering magnets on the sphere's rolling path to create two stable equilibria, to allow the EH to operate over a broad bandwidth. A theoretical model including impact dynamics is developed to investigate the performance of the EH. The theoretical study shows that the sphere magnet can operate from the intra-well to the chaotic, and to periodic inter-well modes of oscillation, depending on the excitation amplitudes and frequencies. Generally, higher excitation amplitude or reduced magnetic tethering forces results in the periodic inter-well motion. A rotary-translational bistable energy harvesting prototype is fabricated in this work for the first time and tested under different excitation conditions to experimentally validate the numerical model. The harvester effectively operates in the periodic inter-well mode between 1 and 2 Hz at low excitation amplitude (between 0.2 g–0.6 g). A peak output power of 9 mW (1.53 mW RMS) was obtained at 2 Hz and 0.7 g. A wireless sensor node with a temperature sensor, a micro-controller and a Bluetooth module was fully powered by the developed EH, illustrating the ability of the device to realize self-powered sensing in real-time monitoring using ultra-low frequency and low-amplitude energy sources. Future work includes system integration for a compact self-powered-sensing system and enhancement of the EH's performance with other dynamics such as multi-stability and parametric resonance for long-term self-monitoring applications, especially for cases where the available energy sources is with ultra-low frequency and excitation amplitude.

Data availability statement

All data that support the findings of this study are included within the article (and any supplementary files).

Acknowledgments

The authors thank the support by the Research Grant (RGS\R2\202148) and the International Exchanges Grant (IEC\NSFC\211070) funded by the Royal Society, UK.

ORCID iD

Hailing Fu  <https://orcid.org/0000-0002-7557-3853>

References

- [1] Khalil N, Abid M R, Benhaddou D and Gerndt M 2014 Wireless sensors networks for internet of things 2014 *IEEE 9th Int. Conf. on Intelligent Sensors, Sensor Networks and Information Processing (ISSNIP)* (IEEE) pp 1–6
- [2] Fu H, Khodaei Z S and Aliabadi M H F 2018 *IEEE Internet Things J.* **6** 1183–92
- [3] Pinar Y, Zuhair A, Hamad A, Resit A, Shiva K and Omar A 2016 Wireless sensor networks (WSNs) 2016 *IEEE Long Island Systems, Applications and Technology Conf. (LISAT)* (IEEE) pp 1–8
- [4] Majid A Y, Schilder P and Langendoen K 2020 Continuous sensing on intermittent power 2020 *19th ACM/IEEE Int. Conf. on Information Processing in Sensor Networks (IPSN)* (IEEE) pp 181–92
- [5] Duan Y, Luo Y, Li W, Pace P and Fortino G 2018 Software defined wireless sensor networks: a review 2018 *IEEE 22nd Int. Conf. on Computer Supported Cooperative Work in Design (CSCWD)* (IEEE) pp 826–31
- [6] Penella M T, Albasa J and Gasulla M 2009 Powering wireless sensor nodes: primary batteries versus energy harvesting 2009 *IEEE Instrumentation and Measurement Technology Conf.* (IEEE) pp 1625–30
- [7] Mitcheson P D, Yeatman E M, Rao G K, Holmes A S and Green T C 2008 *Proc. IEEE* **96** 1457–86
- [8] Wang J, Geng L, Ding L, Zhu H and Yurchenko D 2020 *Appl. Energy* **267** 114902
- [9] Zhang J, Yu X, Zhao W and Qu D 2021 *J. Phys. D: Appl. Phys.* **54** 365501
- [10] Fang S, Miao G, Chen K, Xing J, Zhou S, Yang Z and Liao W-H 2022 *Energy* **241** 122833
- [11] Fu H, Mei X, Yurchenko D, Zhou S, Theodossiades S, Nakano K and Yeatman E M 2021 *Joule* **5** 1074–118
- [12] Siang J, Lim M and Leong M S 2018 *Int. J. Energy Res.* **42** 1866–93
- [13] Kokkinopoulos A, Vokas G and Papageorgas P 2014 *Energy Proc.* **50** 1070–85
- [14] Wang J, Zhang C, Yurchenko D, Abdelkefi A, Zhang M and Liu H 2022 *Energy* **239** 122203
- [15] Rantz R and Roundy S 2017 *Energy Harvest. Syst.* **4** 67–76
- [16] Wu H, Tao Z, Li H, Xu T, Wang W and Sun J 2022 *J. Phys. D: Appl. Phys.* **55** 145502
- [17] Blad T W and Tolou N 2019 *J. Intell. Mater. Syst. Struct.* **30** 2436–46
- [18] Hu G, Lan C, Tang L, Zhou B and Yang Y 2022 *Mech. Syst. Signal Process.* **168** 108724
- [19] Hu G, Lan C, Liang J, Tang L and Zhao L 2022 *J. Intell. Mater. Syst. Struct.* **33** 2000–16

- [20] Wu Y, Qiu J, Kojima F, Ji H, Xie W and Zhou S 2019 *AIP Adv.* **9** 045312
- [21] Fu H and Yeatman E M 2017 *Energy* **125** 152–61
- [22] Jia Y 2020 *J. Intell. Mater. Syst. Struct.* **31** 921–44
- [23] Wang Y, Li S, Wang P, Gao M, Ouyang H, He Q and Wang P 2021 *Smart Mater. Struct.* **30** 125012
- [24] Li K, Yang Z and Zhou S 2020 *Smart Mater. Struct.* **29** 085045
- [25] Andò B, Baglio S, Bulsara A and Marletta V 2014 *Sens. Actuators A* **211** 153–61
- [26] Pellegrini S P, Tolou N, Schenk M and Herder J L 2013 *J. Intell. Mater. Syst. Struct.* **24** 1303–12
- [27] Tran N, Ghayesh M H and Arjomandi M 2018 *Int. J. Eng. Sci.* **127** 162–85
- [28] Yildirim T, Ghayesh M H, Li W and Alici G 2017 *Renew. Sustain. Energy Rev.* **71** 435–49
- [29] Mei X, Zhou R, Fang S, Zhou S, Yang B and Nakano K 2021 *Mech. Syst. Signal Process.* **152** 107424
- [30] Carneiro P, dos Santos M P S, Rodrigues A, Ferreira J A, Simões J A O, Marques A T and Kholkin A L 2020 *Appl. Energy* **260** 114191
- [31] Liu H, Fu H, Sun L, Lee C and Yeatman E M 2021 *Renew. Sustain. Energy Rev.* **137** 110473
- [32] Bi M, Wu Z, Wang S, Cao Z, Cheng Y, Ma X and Ye X 2020 *Nano Energy* **75** 104968
- [33] Iqbal M, Nauman M M, Khan F U, Abas P E, Cheok Q, Iqbal A and Aissa B 2021 *Int. J. Energy Res.* **45** 65–102
- [34] Priya S, Song H C, Zhou Y, Varghese R, Chopra A, Kim S G, Kanno I, Wu L, Ha D S and Ryu J et al 2017 *Energy Harvest. Syst.* **4** 3–39
- [35] Fu H and Yeatman E M 2018 *Smart Mater. Struct.* **27** 084003
- [36] Zhang X, Gao S, Li D, Jin L, Wu Q and Liu F 2018 *Appl. Phys. Lett.* **112** 163902
- [37] Li X, Yu K, Upadrashta D and Yang Y 2019 *J. Phys. D: Appl. Phys.* **52** 235501
- [38] Yi Z, Hu Y, Ji B, Liu J and Yang B 2018 *Appl. Phys. Lett.* **113** 183901
- [39] Fu H, Sharif-Khodaei Z and Aliabadi F 2019 *Appl. Phys. Lett.* **114** 143901
- [40] Yang Y, Shen Q, Jin J, Wang Y, Qian W and Yuan D 2014 *Appl. Phys. Lett.* **105** 053901
- [41] Mohanty A, Parida S, Behera R K and Roy T 2019 *J. Adv. Dielectr.* **9** 1930001
- [42] Poulin G, Sarraute E and Costa F 2004 *Sens. Actuators A* **116** 461–71
- [43] Tan Y, Dong Y and Wang X 2016 *J. Microelectromech. Syst.* **26** 1–16
- [44] Zhang Y, Luo A, Wang Y, Dai X, Lu Y and Wang F 2020 *Appl. Phys. Lett.* **116** 053902
- [45] Yan B, Yu N, Zhang L, Ma H, Wu C, Wang K and Zhou S 2020 *Smart Mater. Struct.* **29** 025022
- [46] Fan K, Zhang Y, Liu H, Cai M and Tan Q 2019 *Renew. Energy* **138** 292–302
- [47] Halim M A, Cho H and Park J Y 2015 *Energy Convers. Manage.* **106** 393–404
- [48] Halim M A, Cho H, Salauddin M and Park J Y 2016 *Sens. Actuators A* **249** 23–31
- [49] Tao Z, Wu H, Li H, Li H, Xu T, Sun J and Wang W 2020 *J. Phys. D: Appl. Phys.* **53** 495503
- [50] Fu H, Theodossiadis S, Gunn B, Abdallah I and Chatzi E 2020 *Nonlinear Dyn.* **101** 2131–43
- [51] Yung K W, Landecker P B and Villani D D 1970 *Magn. Electr. Sep.* **9** 39–52
- [52] Moss S D, Hart G A, Burke S K and Carman G P 2014 *Appl. Phys. Lett.* **104** 033506
- [53] Haron A and Ismail K 2012 Coefficient of restitution of sports balls: a normal drop test *IOP Conf. Ser.: Mater. Sci. Eng.* **36** 012038
- [54] Suryavanshi N B, Viswavidharan Reddy K and Chandrika V R 2019 Direction finding capability in bluetooth 5.1 standard *Int. Conf. on Ubiquitous Communications and Network Computing* (Springer) pp 53–65